



Compositional variations in highly active PtSn/Al₂O₃ catalysts derived from molecular complexes

Chaokai Xu^{a,1}, Shengdong Tan^{a,1}, Yaxin Tang^{a,b,1}, Shibo Xi^{c,*}, Bingqing Yao^a, Austin Wade^d, Binbin Zhao^a, Shangchen Lu^a, Yankun Du^a, Mingjiao Tian^{a,e}, Chi He^e, Lu Ma^f, Xingjie Fu^g, Jiwei Shi^g, Jiong Lu^{g,h}, Alexander G.R. Howe^a, Sheng Dai^{i,*}, Guangfu Luo^{b,*}, Qian He^{a,h,**}

^a Department of Material Science and Engineering, College of Design and Engineering, National University of Singapore, 9 Engineering Drive 1, EA #03-09, 117575, Singapore

^b Department of Materials Science and Engineering and Guangdong Provincial Key Laboratory of Computational Science and Material Design, Southern University of Science and Technology, Shenzhen, Guangdong 518055, China

^c Institute of Sustainability for Chemicals, Energy and Environment (ISCE2), Agency for Science, Technology and Research in Singapore (A*STAR), 1 Pesek Road, Jurong Island 627833, Singapore

^d Thermo Fisher Scientific, 5350 NW Dawson Creek Drive, Hillsboro, OR, USA

^e State Key Laboratory of Multiphase Flow in Power Engineering, School of Energy and Power Engineering, Xi'an Jiaotong University, Xi'an 710049, Shaanxi, China

^f National Synchrotron Light Source II (NSLS-II), Brookhaven National Laboratory, Upton, NY 11973, United States

^g Department of Chemistry, National University of Singapore, 12 Science Drive 2, 117549, Singapore

^h Centre for Hydrogen Innovations, National University of Singapore, E8, 1 Engineering Drive 3, 117580, Singapore

ⁱ Key Laboratory for Advanced Materials and Joint International Research Laboratory of Precision Chemistry and Molecular Engineering, School of Chemistry and Molecular Engineering, East China University of Science & Technology, Shanghai 200237, China

ARTICLE INFO

Keywords:

Nanoalloys
Compositional analysis
Propane dehydrogenation
Electron microscopy

ABSTRACT

We investigated the industrially important PtSn/Al₂O₃ catalysts prepared with uniform particle sizes (~ 1 nm) and varied compositions using molecular complexes of Pt(II) and Sn(II). Our best catalyst, with a Sn:Pt ratio of around 2, exhibited a high initial propylene productivity of about 1.1 mol C₃H₆ (g catalyst)⁻¹ h⁻¹. Elaborate electron microscopy studies revealed significant compositional variations in the catalyst, highlighting the practical challenges in achieving or confirming the theoretically predicted optimum Sn:Pt ratio. It is also found that the catalytic activities correlate well with the Pt dispersion, suggesting the structure-insensitive nature of the dehydrogenation reaction applies to these ultrasmall Pt-Sn nanoparticles. The presence of Pt-rich particles in the catalysts did not produce noticeable degradations in the reaction selectivity, indicating a wide composition range for Pt-Sn nanoparticles to be effective at the 1 nm size range. These findings emphasize the importance of detailed analysis of compositional distributions for understanding and optimizing nanoalloys.

1. Introduction

Alloyed nanoparticles or nanoalloys are widely utilized as catalysts in academic research and industrial applications, owing to their often-superior catalytic activities and tunable compositions and morphologies (e.g., core-shell), if compared to monometallic counterparts [1,2]. Meanwhile, the controlled synthesis of nanoalloys can be challenging as it requires precise control over the dispersion of two or more metals.

Electron microscopy has been indispensable in developing synthesis protocols by providing chemical information of individual alloyed nanoparticles at the atomic scale [3]. However, composition distribution among particles, analogous to the routinely reported particle size distribution (PSD) in the case of monometallic catalyst, is rarely assessed in the research of nanoalloy catalysts. A handful of studies [4–8] that have performed such analyses often report substantial compositional variations among particles, complicating the correlation between observed

* Corresponding authors.

** Corresponding author at: Department of Material Science and Engineering, College of Design and Engineering, National University of Singapore, 9 Engineering Drive 1, EA #03-09, 117575, Singapore.

E-mail addresses: xi_shibo@isce2.a-star.edu.sg (S. Xi), shengdai@ecust.edu.cn (S. Dai), luogf@sustech.edu.cn (G. Luo), mseheq@nus.edu.sg (Q. He).

¹ These authors contributed equally

catalytic properties and specific particle composition. In other cases, the lack of comprehensive compositional analysis often hinders a clear understanding of the synthesis-structure-property relationships in nanocatalysts.

A good example of the complex relationship between composition and catalytic performance is observed in PtSn/Al₂O₃ catalysts, commonly employed in industrial propane dehydrogenation (PDH) processes [9]. While it's recognized that the addition of Sn enhances propylene selectivity and reduces coking, the mechanisms through which Sn improves the Pt catalyst remain elusive [10]. Proposed theories include Sn's potential roles in sterically isolating Pt sites [11,12], electronically influencing Pt to expedite propylene desorption and deter coking [13,14], serving as nucleation sites during catalyst synthesis and regeneration [15,16], and quenching acidic sites on the support [17,18]. Additionally, Sn was also proposed as active sites in the PDH reaction [19]. Controlled synthesis of Pt-Sn catalysts is challenging, and compositional distributions of Pt-Sn nanoparticles are often not reported for catalysts prepared using different methods. The ambiguities are evidenced as different reported optimum Sn:Pt ratios, ranging at least from about 1:3 [20] to about 6:1 [21] (Fig. S1 and Table S1).

In this work, we investigated Pt-Sn catalysts prepared from pre-formed anionic complexes of Pt(II) and Sn(II) [22,23]. This method led to uniform particle sizes of around 1 nm with various Sn:Pt ratios, enabling us to search for an optimum composition. Our most effective catalyst, with a Sn:Pt ratio of approximately 2, exhibited an initial mass-specific propylene productivity of about 1.1 mol C₃H₆ (g catalyst)⁻¹ h⁻¹, a figure that was among the highest reported values. The catalyst also displayed a low deactivation rate of 0.009 h⁻¹ under optimized reaction conditions. Detailed characterizations, particularly electron microscopy studies, revealed significant compositional variations within this optimum catalyst. The Sn contents within individual nanoparticles were found ranging from about 30–70%, which was almost identical to the composition distribution observed in the catalyst prepared without pre-formed complexes via a more conventional impregnation method.

The observed compositional variations in PtSn/Al₂O₃ catalysts highlighted the experimental challenges in achieving or confirming the theoretically predicted optimum Sn:Pt ratio. Interestingly, we found that the observed catalytic activities correlated well with the Pt dispersions, which was in line with conventional wisdoms of the structural insensitive nature of the dehydrogenation reaction [24]. In addition, we did not observe noticeable degradations in reaction selectivity despite the presence of Pt-rich particles in the catalysts. This suggested that there might be a wide composition range for Pt-Sn nanoparticles to be effective, at least at this 1 nm size range. Our density functional theory (DFT) calculations and molecular dynamics (MD) simulations showed that these small Pt-Sn nanoparticles exhibited dynamic structures, and similar active sites could exist in particles with different compositions. These new and complex insights of the industrially important Pt-Sn/Al₂O₃ catalysts were made possible only because of the detailed compositional analysis from electron microscopy.

2. Experimental section

2.1. Catalyst preparation

The A-series of Pt-Sn/Al₂O₃ catalysts were prepared by loading pre-formed anionic complexes of Pt(II) and Sn(II) complexes onto Al₂O₃ using an electrostatic adsorption method in an organic media, followed by *in situ* heat treatment in pure H₂ at 550 °C for an hour, before the PDH reaction. To prepare the molecular complex, K₂PtCl₄ (Aladdin, ≥99.9% metals basis) was dissolved in deionized water, and then transferred to CH₂Cl₂ (VWR, ≥99%) with NBu₄Br (Sigma Aldrich, ≥98%). The molar amount of NBu₄Br was 2.2 times the amount of Pt to enable efficient phase transfer. SnCl₂·2 H₂O (Aladdin, ≥99.99% metals basis) was dissolved in tetrahydrofuran (VWR, ≥99.5%). Pt (0.0067 M) and Sn (0.09

M) solution were mixed to attain various Sn:Pt molar ratio, from 0.5 to 3. Color changes took place immediately. After 30 min' stirring to stabilize the solution, a certain amount of Al₂O₃ powder (Sigma Aldrich, 13 nm primary particle size, BET surface area 109.5 m²/g, 99.8% trace metals basis) was added and the mixture was stirred at room temperature for 24 h. During this process, the Pt-Sn complexes could be loaded onto Al₂O₃ through adsorption. Centrifugation was applied to separate the catalyst and organic solvent. Finally, the obtained catalyst was dried and stored in a vacuum desiccator. Catalysts with a series of Sn:Pt molar ratios (i.e., 1:1, 2:1 and 4:1) were prepared. These catalysts were denoted A-Pt_xSn_y/Al₂O₃, with the x and y indicating the Sn:Pt ratio in the catalyst measured by ICP-OES. A Pt-only catalyst (A-Pt/Al₂O₃) was synthesized through the same procedure mentioned above only adding K₂PtCl₄ and no Sn precursors. A Sn-only catalyst (A-Sn/Al₂O₃) was obtained by impregnation of SnCl₂ in tetrahydrofuran to ensure successful loading of Sn.

Another Pt₁Sn₂/Al₂O₃ catalyst (B-Pt₁Sn₂/Al₂O₃) was synthesized by impregnation in aqueous phase. Bimetallic complex could form between H₂PtCl₆·6 H₂O (Aladdin, AR, Pt≥37.5%) and Sn(II) from SnCl₂·2 H₂O (Sigma-Aldrich, 98%). 1 M HCl was added to fully dissolve the complex. The Pt-Sn solution was mixed with support and water was gradually evaporated under heating and stirring. After drying the mixture to paste state, it was further dried and stored in vacuum desiccator. The catalyst would also undergo *in situ* heat treatment in pure H₂ at 550 °C for an hour, before the PDH reaction.

The third Pt₁Sn₂/Al₂O₃ catalyst (C-Pt₁Sn₂/Al₂O₃) was synthesized with similar procedures to B-Pt₁Sn₂/Al₂O₃. The differences were that Pt from H₂PtCl₆·6 H₂O (Aladdin, AR, Pt≥37.5%) and Sn(IV) from SnCl₄·5 H₂O (Sigma Aldrich, 98%) stayed isolated, and no additional HCl was needed. The catalyst would also undergo *in situ* heat treatment in pure H₂ at 550 °C for an hour, before the PDH reaction.

2.2. Catalyst characterizations

UV-Vis absorption spectra of Pt-Sn solution were measured by Shimadzu UV-1900 UV-Vis spectrometer, from 200 to 600 nm, using CH₂Cl₂ as the reference. Pt-Sn solution was diluted with CH₂Cl₂ before tests to produce signal in a reasonable intensity range.

UV-Vis diffuse reflectance spectra (DRS) of Pt-Sn species supported on Al₂O₃ were collected by Shimadzu UV-2600 UV-Vis spectrometer with integrating sphere. Dried Pt-Sn/Al₂O₃ powder without heat treatment was spread on the white BaSO₄ background and absorbance spectra from 200 to 800 nm were recorded.

Specific surface area of Al₂O₃ was calculated from N₂ adsorption isotherms on Micromeritics ASAP 2460, using BET (Brunauer, Emmett and Teller) method.

X-ray diffraction (XRD) patterns of Al₂O₃ and Pt-Sn catalysts after reduction were recorded on Bruker D-8 Advance. The range of 2θ was from 5° to 60°.

Elemental composition of catalysts was determined by Perkin Elmer Avio 500 inductively coupled plasma optical emission spectroscopy (ICP-OES). Solid samples were digested with a mixture of HCl, HNO₃ and HF.

NH₃ temperature programmed desorption (TPD) experiments were conducted on Quantachrome Autosorb IQ-C-AG for Pt-Sn catalysts and Al₂O₃ support. Samples were *in situ* reduced by pure H₂ at 550 °C for an hour and then cooled down to 50 °C in He. After NH₃ adsorption at 50 °C, temperature was ramped to 800 °C at 10 °C/min rate to record NH₃ desorption signal by TCD.

CO diffuse reflectance FT-IR spectra (DRIFTS) were acquired on Nicolet iS50 FT-IR spectrometer. The catalyst was *ex situ* reduced by pure H₂ at 550 °C for an hour in advance, and *in situ* reduced by pure H₂ at 400 °C for 1 h to remove passivation layer. After reduction, the sample was cooled down to 30 °C in H₂ atmosphere, and then the cell was flushed with Ar. Background was collected at 30 °C in Ar. Afterwards, 5% CO/He was flowed through the cell until adsorption saturation

according to spectra. Finally, the cell was flushed with Ar to record the signal from residual adsorbed CO.

Pt dispersity was characterized by CO chemisorption on Quantachrome Autosorb IQ-C-AG. The catalyst was *in situ* reduced by pure H₂ at 550 °C for an hour, followed by He flow at 550 °C for two hours. After cooling down to 50 °C in He atmosphere, CO pulse titration was conducted.

In situ X-ray Absorption Fine Structure (XAFS) study was carried out at the Singapore Synchrotron Light Source (SSLS) [25]. Fresh catalysts were pelletized and *in situ* reduced by pure H₂ at 550 °C in a micro-reactor. Then the sample is then cooled down to the room temperature in the same pure H₂ flow before the Pt L_{III} (11564 eV) spectra were taken in the transmission mode. Several scans were acquired to increase signal-to-noise ratio and ensure reproducibility of data. Pt foil and PtO₂ were used as references. Data analysis was done on Athena and Artemis software developed by B. Ravel and M. Newville [26]. Details of the data processing procedures can be found in Text S1.

Images of Pt-Sn particles were acquired on a JEOL JEM-ARM200CF aberration-corrected scanning transmission electron microscope (STEM) at National University of Singapore, operated at 200 kV, and a Thermofisher Themis Z at East China University of Science and Technology, operated at 300 kV. The size distribution of particles was determined from high-angle annular dark field (HAADF) images.

Elemental composition of individual particles was obtained from X-EDS maps acquired on the Thermofisher Themis Z operated at 60 kV at East China University of Science and Technology, China. The microscope equipped with Super-X EDS detection system with four 30 mm² Silicon Drift Detectors (SDDs), with a combined collection angle of about 0.7 steradians. In a typical EDS-SI acquisition, probe current was set at around 100 pA, pixel time is 64 μs, frame time is 1.2 s, and the total data set contains about 3000 frames. Some preliminary results were obtained using the Thermofisher Spectra Ultra microscope at the Hillsboro

each. The mixture was supported by quartz wool in a quartz tube with 7 mm inner diameter.

Prior to reaction, the catalyst was heated to 550 °C at a 10 °C/min ramp rate and retained for 1 h under 20 mL/min pure H₂ flow. After reduction, the inlet gas was switched to 30 mL/min C₃H₈ (WHSV = 165 h⁻¹). WHSV (weight hourly space velocity) was defined as the mass flow rate of C₃H₈ divided by the mass of catalyst. The stability of the catalyst was tested with 5 mL/min C₃H₈, 5 mL/min H₂ and 15 mL/min Ar (WHSV = 27.5 h⁻¹). Kinetics measurements were conducted over the range of 480–550 °C. Each time 5 mg catalyst was tested with 30 mL/min C₃H₈ (WHSV = 660 h⁻¹) to make sure the reaction condition stayed far from thermodynamic limit.

The composition of outlet gas was analyzed by online gas chromatography (Agilent 990 Micro GC) equipped with parallel PPQ and MS5A columns and corresponding thermal conductivity detectors, using He and Ar as carrier gas, respectively. Volumetric fractions of C₃H₈, C₃H₆ and potential by-products, including CH₄, C₂H₆, C₂H₄ and C₂H₂, were determined from external standard calibration. Conversion of C₃H₈ and selectivity to C₃H₆ were calculated by Eqs. 1 and 2. [Gas] represented the molar flow rate of the gaseous components. Carbon mass balance was defined as the ratio of C atoms in outlet and inlet gas (Eq. 3). Throughout the analysis, carbon mass balance was over 97%. Yield of C₃H₆ was defined as the product of conversion of C₃H₈ and selectivity to C₃H₆ (Eq. 4). Pt-specific and mass-specific activities were defined as the molar flow rate of C₃H₆ in outlet gas divided by the mass of Pt or the mass of catalyst, respectively, as shown in Eq. (5). Deactivation of catalysts was characterized according to pseudo first order model (Eq. 6), where X and X₀ represented conversion at time t and the beginning of reaction, respectively. Deactivation coefficient *k_d* was obtained by liner fitting. TOF (turn over frequency) was calculated by exposed Pt site in Eq. 7.

$$\text{Conversion} = \frac{3 \times [\text{C}_3\text{H}_6]_{\text{out}} + 2 \times [\text{C}_2\text{H}_6]_{\text{out}} + 2 \times [\text{C}_2\text{H}_4]_{\text{out}} + 2 \times [\text{C}_2\text{H}_2]_{\text{out}} + 1 \times [\text{CH}_4]_{\text{out}}}{3 \times [\text{C}_3\text{H}_8]_{\text{out}} + 3 \times [\text{C}_3\text{H}_6]_{\text{out}} + 2 \times [\text{C}_2\text{H}_6]_{\text{out}} + 2 \times [\text{C}_2\text{H}_4]_{\text{out}} + 2 \times [\text{C}_2\text{H}_2]_{\text{out}} + 1 \times [\text{CH}_4]_{\text{out}}} \quad (1)$$

$$\text{Selectivity} = \frac{3 \times [\text{C}_3\text{H}_6]_{\text{out}}}{3 \times [\text{C}_3\text{H}_6]_{\text{out}} + 2 \times [\text{C}_2\text{H}_6]_{\text{out}} + 2 \times [\text{C}_2\text{H}_4]_{\text{out}} + 2 \times [\text{C}_2\text{H}_2]_{\text{out}} + 1 \times [\text{CH}_4]_{\text{out}}} \quad (2)$$

$$\text{Carbon mass balance} = \frac{3 \times [\text{C}_3\text{H}_8]_{\text{out}} + 3 \times [\text{C}_3\text{H}_6]_{\text{out}} + 2 \times [\text{C}_2\text{H}_6]_{\text{out}} + 2 \times [\text{C}_2\text{H}_4]_{\text{out}} + 2 \times [\text{C}_2\text{H}_2]_{\text{out}} + 1 \times [\text{CH}_4]_{\text{out}}}{3 \times [\text{C}_3\text{H}_8]_{\text{in}}} \quad (3)$$

NanoPort, United States, operated at 80 kV. This microscope had the Ultra-X EDS detectors with a collection angle larger than 4 steradians. More details of the EDS quantification process could be found in Text S2.

To improve the conductivity of the sample and minimize charging effects during electron microscopy studies, a thin layer of carbon coating with a nominal thickness of 3 nm was carried out using the LEICA EM ACE200. The sample was put on a plastic petri dish when performing the coating. The coater uses thin carbon threads and the sample was located a few centimeters away. The temperature of the sample did not raise significantly as evidenced by the integrity of the plastic petri dish. We also examined the sample before and after the carbon coating using AC-STEM (data not shown), no observable changes can be found in terms of particle sizes.

2.3. Catalytic property measurement

The performance of the catalysts in the PDH reaction was measured using a fixed bed downflow reactor built in-house. In a typical experiment, 0.02 g catalyst was mixed with 0.98 g sand (Sigma Aldrich, 50–70 mesh particle size), and sandwiched by another two layers of sand, 0.5 g

$$\text{Yield}(\%) = \text{Conversion} \times \text{Selectivity} \quad (4)$$

$$\text{Pt specific activity} = \frac{[\text{C}_3\text{H}_6]_{\text{out}}}{m_{\text{Pt}}} \quad (5)$$

$$\text{Mass specific activity} = \frac{[\text{C}_3\text{H}_6]_{\text{out}}}{m_{\text{catalyst}}} \quad (5)$$

$$\text{Deactivation model } k_d t = \ln\left(\frac{1-X}{X}\right) - \ln\left(\frac{1-X_0}{X_0}\right) \quad (6)$$

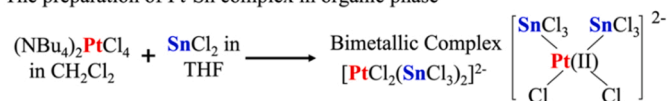
$$\text{Turn over frequency } (s^{-1}) = \frac{[\text{C}_3\text{H}_6]_{\text{out}}}{n_{\text{Pt}} \bullet \text{dispersity}} \quad (7)$$

2.4. Computation methods

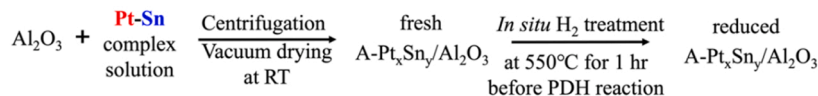
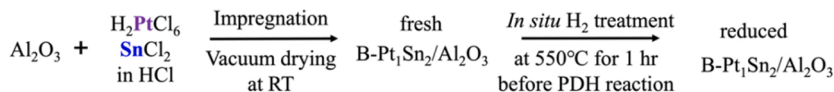
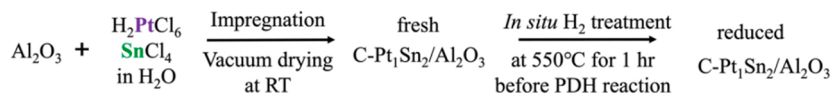
The density functional theory (DFT) calculations were performed using the Vienna Ab initio Simulation Package (VASP) [27–29], together with the Perdew-Burke-Ernzerhof (PBE) exchange-correlation functional. The van der Waals corrections were included through the DFT-D3

A-Pt_xSn_y/Al₂O₃

Step 1 – The preparation of Pt-Sn complex in organic phase



Step 2 – Support the molecular complex and heat treatment

**B-Pt₁Sn₂/Al₂O₃****C-Pt₁Sn₂/Al₂O₃****Scheme 1.** Synthesis procedures of Pt-Sn bimetallic complexes (e.g., Pt₁Sn₂), A-Pt_xSn_y/Al₂O₃, B-Pt₁Sn₂/Al₂O₃ and C-Pt₁Sn₂/Al₂O₃. Red: Pt(II); blue: Sn(II); purple: Pt(IV); green: Sn(IV).**Table 1**Initial PDH activity of the Pt-Sn/Al₂O₃ catalysts involved in this work. Reaction conditions: 20 mg catalyst, 550 °C, 30 mL/min pure C₃H₈, WHSV = 165 h⁻¹.

| Catalyst | Pt (wt%)* | Sn:Pt** | C ₃ H ₈ Conversion (%) | C ₃ H ₆ Selectivity (%) | Pt specific activities (mol C ₃ H ₆ g _{Pt} ⁻¹ h ⁻¹) | Mass specific activities (mol C ₃ H ₆ g _{catalyst} ⁻¹ h ⁻¹) |
|---|-----------|---------|--|---|---|---|
| A-Pt/Al ₂ O ₃ | 0.52 | 0 | 7.91 | 97.0 | 55.2 | 0.29 |
| A-Pt ₁ Sn ₁ /Al ₂ O ₃ | 0.56 | 0.97 | 26.85 | 99.6 | 179 | 1.0 |
| A-Pt ₁ Sn ₂ /Al ₂ O ₃ | 0.55 | 2.30 | 29.43 | 99.8 | 200 | 1.1 |
| A-Pt ₁ Sn ₄ /Al ₂ O ₃ | 0.62 | 3.92 | 25.15 | 99.8 | 152 | 0.94 |
| B-Pt ₁ Sn ₂ /Al ₂ O ₃ | 0.57 | 2.02 | 26.57 | 99.8 | 174 | 0.99 |
| C-Pt ₁ Sn ₂ /Al ₂ O ₃ | 0.58 | 2.01 | 20.83 | 99.9 | 134 | 0.78 |
| A-Sn/Al ₂ O ₃ | (Sn) 0.86 | - | 0.47 | 62.8 | - | 0.01 |

* The loadings of Pt and Sn were determined by ICP-OES.

** Sn:Pt atomic ratios were calculated from the metal loadings.

method [30] and the pseudopotentials were described by the projected augmented wave method [31]. A gamma point was used to sample the Brillouin zone. The initial configurations of Pt₁₅Sn₁₅ and Pt₁₀Sn₂₀ clusters were constructed from the bulk PtSn (P63/mmc) and PtSn₂ (Fm-3 m). MD simulations based on the on-the-fly machine learning force fields were performed in the canonical ensemble using a Nose-Hoover thermostat at 873 K for 30 ps with a time step of 1 fs [32–34]. Geometry optimizations were executed with an energy tolerance of 1.0 × 10⁻⁵ eV and a force tolerance of 0.01 eV Å⁻¹. Transition state search was carried out with the climbing nudged elastic band (cNEB) method and the initial structures were generated by the ASBA method [35,36]. The plane-wave energy cut-off was set to 328 eV for geometry optimization and cNEB calculations and 311 eV for MD simulations. Gibbs free energy corrections (Table S2) were added to the adsorption/desorption steps in the energy diagram. The charge state on each atom was obtained using the Bader charge analysis [37,38].

3. Results and discussion**3.1. Preparation of PtSn/Al₂O₃ catalysts with controlled particle sizes and Sn:Pt ratios**

We aimed to synthesize well-defined PtSn catalysts from bimetallic complexes to enable more controlled deposition of Pt and Sn precursors with adjustable compositions. Previous works [21,39] typically involved the use of a Pt(IV) precursor (e.g., H₂PtCl₆) and a Sn(II) precursor (e.g., SnCl₂) in an aqueous solution of HCl to form such complexes. However, we encountered challenges with this method particularly when aiming for higher Sn:Pt ratios (e.g., 2:1 or higher), as it often led to uncontrolled precipitations, limiting our ability to achieve the desired range of catalyst compositions. Therefore, we developed a different approach utilizing organic solvents for the preparation of molecular complexes and catalysts. As illustrated in Scheme 1, a Pt(II) precursor (i.e., K₂PtCl₄) was first dissolved in CH₂Cl₂ and a Sn(II) precursor (i.e., SnCl₂) would be added. The color of the Pt solution, initially light yellow, gradually darkened and turned red with increasing

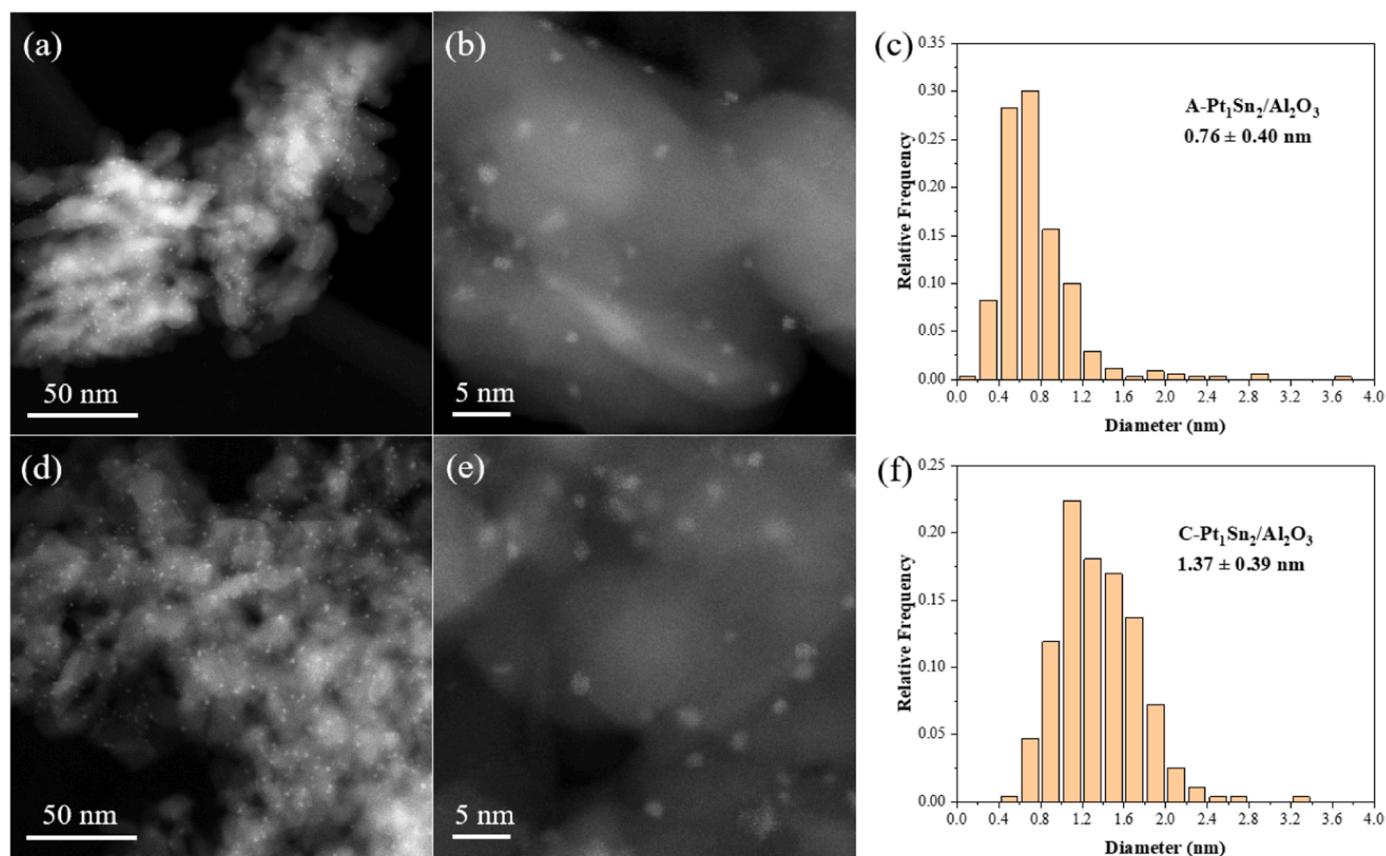


Fig. 1. Representative HAADF-STEM images and the corresponding particle size distributions of (a-c) the reduced A-Pt₁Sn₂/Al₂O₃ catalysts and (d-f) the C-Pt₁Sn₂/Al₂O₃ catalysts. Additional images of the two catalysts can be found in Figs. S4 and S5, respectively.

amounts of Sn, indicating the interaction between Pt and Sn species. UV-Vis absorption spectroscopy was employed to analyze the Pt-Sn mixed solution with varying Sn:Pt molar ratios, as shown in Fig. S2. The shoulder peak centered at 258 nm in Sn spectra was shifted to higher wavelength because of the existence of Pt. According to the work by Baronetti et al. [40], this feature at around 258 nm could be ascribed to the charge transfer from (SnCl₃)⁻¹ to Pt(II) in the bimetallic complex structure, and another peak around 360 nm could result from the d-d transition. The emergence of these peaks implied that the solution contained coordinated Pt-Sn complexes.

Next, the desired amount of Al₂O₃ was introduced to the mixture and the anionic Pt-Sn complexes would be selectively adsorbed. The UV-Vis spectra of the Pt or Pt-Sn loaded material (Fig. S3) exhibited significantly increased absorbance in the visible range compared to the white Al₂O₃ support. This enhancement may be attributed to the charge transfer between the metal species and the oxygen atoms from the support [41]. In addition, the spectra shown in Fig. S3 displayed features similar to those observed from the Pt-Sn complexes (Fig. S2) in CH₂Cl₂, such as the peaks around 270 and 360 nm. Given the controlled loading process and the presence of characteristic peaks, it could be inferred that the Pt-Sn complexes were successfully preserved on the Al₂O₃ support.

For comparison purposes, other types of PtSn/Al₂O₃ were also prepared using the same support materials, as shown in Scheme 1 and the method section. B-Pt₁Sn₂/Al₂O₃ represented a catalyst prepared using a more conventional impregnation method, with preformed complex between a Pt(IV) precursor (*i.e.*, H₂PtCl₆) and a Sn(II) precursor (*i.e.*, SnCl₂) in an 1 M HCl solution. C-Pt₁Sn₂/Al₂O₃ was another catalyst prepared with impregnation method without the Pt and Sn forming complexes in the solution, since a Pt(IV) precursor (*i.e.*, H₂PtCl₆) and a Sn(IV) precursor (*i.e.*, SnCl₄) were used. The metal loadings of all the catalysts were measured using ICP-OES (Table 1). No potassium (K) was

detected in the A-series catalysts. The metal loadings of B-Pt₁Sn₂/Al₂O₃ and C-Pt₁Sn₂/Al₂O₃ catalysts were adjusted to be as close as possible to the metal loadings of A-Pt₁Sn₂/Al₂O₃ (*i.e.*, 0.55 wt% Pt). A-Pt₁Sn₂/Al₂O₃ was selected as the benchmark due to its superior catalytic performance, as elaborated in the next section.

Since the fresh catalysts would be heat treated in pure H₂ inside the reactor at 550 °C before being tested for PDH reaction, we focused on characterizing the catalysts after the H₂ heat treatment as it should best represent the catalyst morphology at the beginning of the reaction. Since Sn metal melts at about 232 °C, we went to check whether the Sn content would change during heat treatment or the PDH reaction both at 550 °C. To do that, we examined the metal loadings of the catalysts before and after the heat treatment at 550 °C in pure H₂ for 1 h using Inductively Coupled Plasma Optical Emission spectroscopy (ICP-OES). As shown in Table S3, no change in the Sn loading could be detected. Representative high angle annular dark field (HAADF) images and the corresponding particle size distributions (PSDs) of the reduced A-Pt₁Sn₂/Al₂O₃ (Fig. 1 (a-c) and Fig. S4) and the reduced C-Pt₁Sn₂/Al₂O₃ (Fig. 1(d-f) and Fig. S5) were shown, and the ones for the rest of the samples were shown in Figs. S6-S9. Except for the reduced B-Pt₁Sn₂/Al₂O₃, all other catalysts showed remarkably uniform particle size distribution with average sizes around 1 nm. The reduced A-Pt₁Sn₂/Al₂O₃ showed the smallest mean particle size of about 0.76 nm. In the case of the reduced B-Pt₁Sn₂/Al₂O₃, large chunks of metal with hundreds of nm in size were observed (Fig. S9), possibly due to the uncontrolled precipitation during the impregnation process as mentioned earlier. Although these big particles provided little surface area for catalytic reactions, their presence meant we had lost control of how much metal would end up being in the particles, making it difficult to establish a structure-property relationship. Hence, we would mostly focus on understanding other catalysts. The HAADF-STEM results were consistent with the XRD results shown in

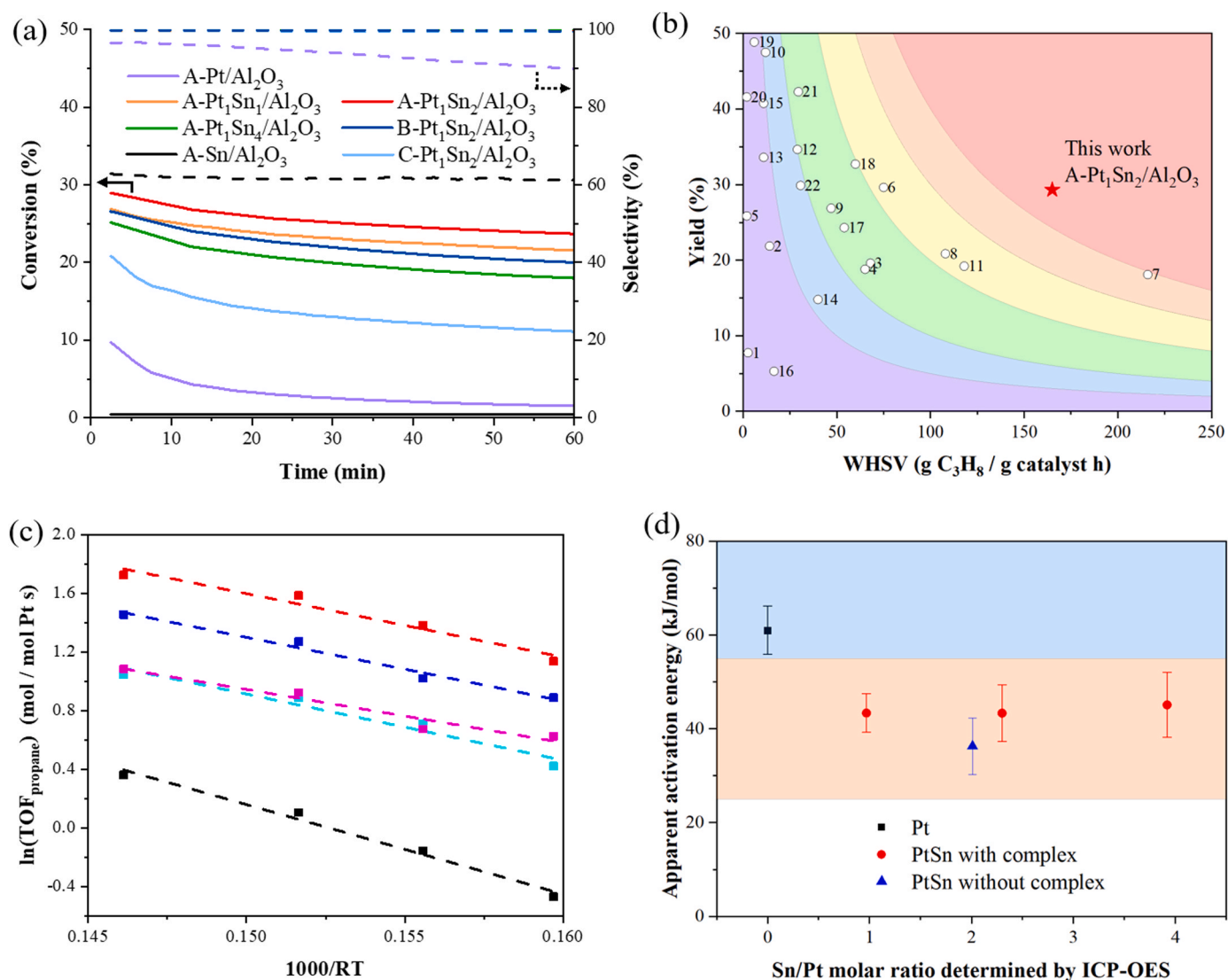


Fig. 2. Propane dehydrogenation performance of the catalysts involved in this work. (a) On stream propane (C₃H₈) conversion (solid lines) and propylene (C₃H₆) selectivity (dashed lines) as a function of time. Reaction conditions: 20 mg catalyst, 550 °C, 30 mL/min pure C₃H₈, WHSV = 165 h⁻¹. (b) Comparison of initial propylene productivities obtained from the A-Pt₁Sn₂/Al₂O₃ catalyst in this study with the best values reported in the literature. The x-axis represents the weight hourly space velocity (WHSV) of propane, The y-axis depicts the propylene yield. The product of WHSV and yield equals mass specific activity, as shown by the contour lines and colored regions. The white circles on the plot correspond to specific publications that can be found in Table S4. (c) Kinetic measurement results, carried out with 5 mg catalyst, 30 mL/min pure C₃H₈, WHSV = 660 h⁻¹ at 480 °C, 500 °C, 520 °C and 550 °C. (d) Apparent activation energy of the catalysts measured in (c). Color code used in (c) and (d): Black - A-Pt/Al₂O₃; Blue - A-Pt₁Sn₁/Al₂O₃; Red - A-Pt₁Sn₂/Al₂O₃; Cyan - A-Pt₁Sn₄/Al₂O₃; Magenta - C-Pt₁Sn₂/Al₂O₃.

Fig. S10, with no visible peaks of Pt or PtSn crystals from the catalysts.

3.2. Catalytic performance of the PtSn/Al₂O₃ catalysts in the PDH reactions

The A-series of the PtSn/Al₂O₃ catalysts prepared in this work exhibited excellent performances in the PDH reaction. It turned out they could only be differentiated when tested in highly demanding reaction conditions. In our standard test, 20 mg of catalysts were loaded into a fix-bed reactor, mixed with 0.98 g sands to prevent any cold spots due to the endothermic nature of the PDH reaction. Pure C₃H₈ feed was used without co-feeding H₂ and the weight hourly space velocity (WHSV) was 165 h⁻¹. The reaction temperature was set at 550 °C. The results were shown in Fig. 2a and Table 1. Selectivity towards propylene measured among the gas phase products was over 99% for all the PtSn/Al₂O₃ catalysts tested. The carbon balance, defined by the gas-phase carbon containing products detected divided by the amount of propane in the input feed, was over 97% in all cases. Pure Pt catalyst was found not as

selective and pure Sn catalyst was largely inactive.

A-Pt₁Sn₂/Al₂O₃ displayed the highest conversion of C₃H₈ and highest productivity of C₃H₆. The initial mass specific activity of A-Pt₁Sn₂/Al₂O₃ was found to be around 1.1 mol C₃H₆ g_{catalyst}⁻¹ h⁻¹, which was about 1.5 times higher than that of C-Pt₁Sn₂/Al₂O₃. This value was also benchmarked with the results reported in literature, demonstrating that the A-Pt₁Sn₂/Al₂O₃ was among the best, as shown in Fig. 2b and Table S4. There were no significant changes in the PtSn particles after 1 h of PDH reaction at 550 °C, as shown in Fig. S11. The A-Pt₁Sn₂/Al₂O₃ catalyst could also operate in conditions that maximized the catalyst stability and the best deactivation coefficient we achieved was 0.009 h⁻¹ when tested while co-feeding 5 mL/min C₃H₈ (WHSV of 27.5 h⁻¹) and 5 mL/min H₂ (Fig. S12).

In order to better show the potential difference between PtSn/Al₂O₃ catalysts with similar particle size but different nominal compositions, we further carried out some kinetics studies [42–44]. Arrhenius plots for various PtSn/Al₂O₃ catalysts were presented in Fig. 2c, based on initial activities measured at different reaction temperatures. As shown in

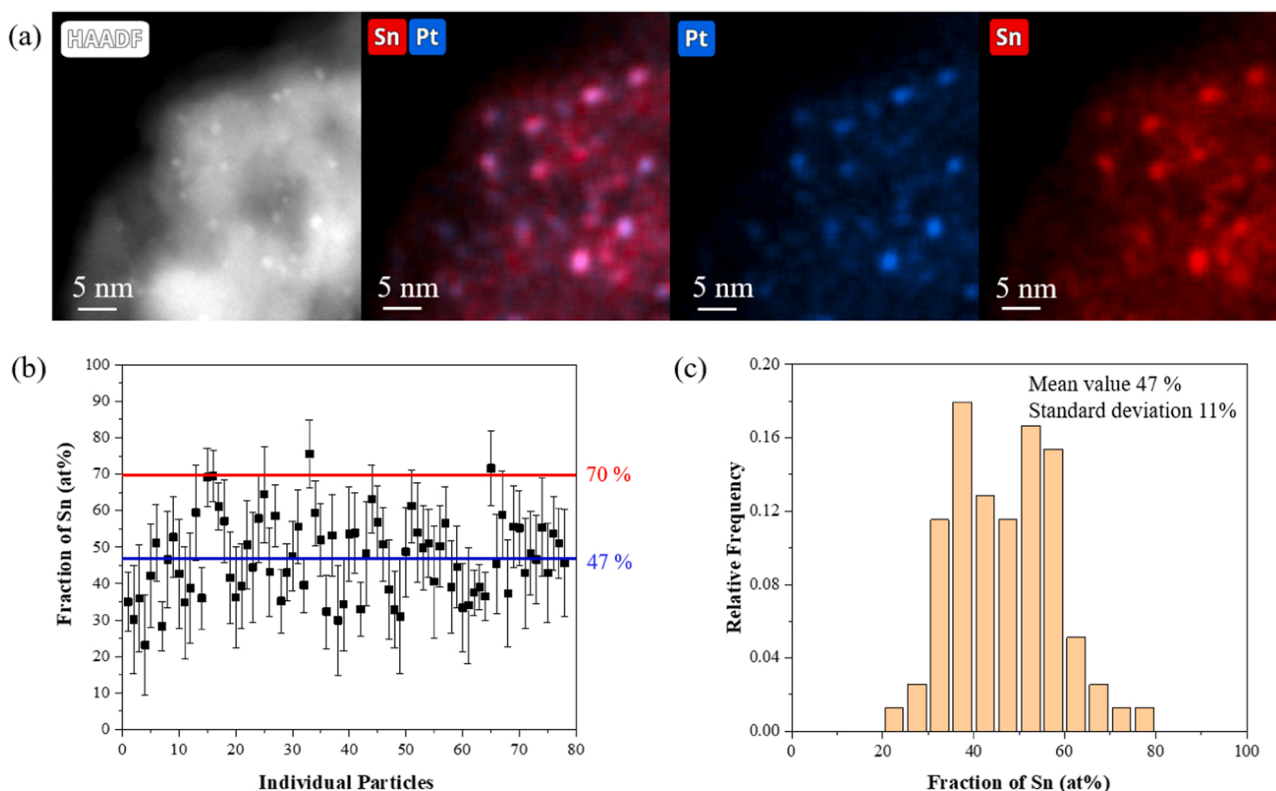


Fig. 3. Compositional analysis of the reduced A-Pt₁Sn₂/Al₂O₃ catalysts using STEM-X-EDS. (a) Representative dataset containing a HAADF image and the corresponding elemental maps obtained from the reduced A-Pt₁Sn₂/Al₂O₃ catalyst. (b) Compositions of individual PtSn nanoparticles (Sn at%) and (c) the corresponding composition distribution histogram. All the particles shown in this plot satisfy the statistical criteria, where both Pt M and Sn L peaks of each particles exceed three times the square root of the corresponding background intensities. (b) and (c) only include the particles with at least 100 photon counts in either Pt M or Sn L peaks. The more inclusive data summary containing the rest of particle spectra can be found in Fig. S18. Red line in (b): the overall Sn composition of the catalyst measured determined by ICP-OES; blue line in (b): average particle composition measured from STEM-X-EDS of individual nanoparticles. The error bars in (b) represent a confidence interval of 99%.

Fig. 2d, all PtSn/Al₂O₃ catalysts exhibited similar apparent activation of about 40 kJ/mol, which was lower than that of the A-Pt/Al₂O₃ (about 60 kJ/mol) (Table S5). Interestingly, no significant differences in apparent activation energy were observed among the PtSn/Al₂O₃ catalysts with different overall Sn:Pt ratios.

3.3. Compositional variations in the PtSn/Al₂O₃ catalysts

We hypothesized that the superior performance of A-Pt₁Sn₂/Al₂O₃ compared to other catalysts was attributed to better control over the nanoparticle compositions, which were closer to the optimum values. While the overall compositions of the catalysts could be reasonably assessed using techniques like ICP-OES, it was crucial to examine the composition distributions among different particles to validate this hypothesis. However, such characterization was rarely conducted in the study of nanoalloys, partly due to the challenges of obtaining sufficient X-ray signals from small particles within the catalysts. This was particularly the case for the PtSn/Al₂O₃ catalysts in this work as the particles are around 1 nm in size. The Al₂O₃ support material, being poorly conductive, was particularly susceptible to beam damage [45].

To overcome these challenges, we coated the sample with a thin layer of carbon about 5–7 nm to improve the conductivity of the Al₂O₃ support. We also used microscopes operated at lower e-beam energies (e.g., 60–80 kV) [7] and equipped with relatively large X-EDS detectors [46] (see the Method section) to improve the efficiencies of X-EDS analysis. These allowed us to obtain enough counts from individual particles around 1 nm in size. We mainly studied the two key samples, A-Pt₁Sn₂/Al₂O₃ (prepared with molecular complexes) and C-Pt₁Sn₂/Al₂O₃ (prepared without molecular complexes).

X-EDS quantification was done via the classic Cliff-Lorimer ratio (K) method [47]. The determination of the k ratio between Pt M peaks and the Sn L peaks was done by probing catalysts particles in large areas, assuming the composition was largely uniform and consistent with the results obtained from ICP-OES (Fig. S13). After that, STEM X-ED spectra imaging at higher resolution was carried out so that individual particles could be visible in the HAADF image simultaneously acquired, and the spectrum from individual particles could be extracted (Fig. S14). In total we obtained spectra of 111 particles from the reduced A-Pt₁Sn₂/Al₂O₃ and 243 particles from the reduced C-Pt₁Sn₂/Al₂O₃. These numbers were comparable to the particle counts typically used for particle size distribution studies. It was important to note that despite the carbon coating, electron beam damage could still be observed (Fig. S15). Hence often we could only select a few particles from a dataset if the damage was found severe. We conducted control experiments to show that continuous electron irradiation did not make any noticeable changes in the particle composition quantification (Fig. S16).

Assuming X-ray emission follows Poisson statistics [47], we were able to obtain statistically significant amount of signal from individual particles in most cases. For a small portion of each sample (i.e., 9.8% from A-Pt₁Sn₂/Al₂O₃ and 7.6% from C-Pt₁Sn₂/Al₂O₃), we only observed significant signals for Pt but not for Sn (Fig. S17). Those particles were presumed to be Pt-rich, but we couldn't get a good estimation of their compositions. For the rest more than 90% of the particles examined, the compositions of individual particles and the composition distributions could be plotted. The particles with at least 100 photon-count in either Pt M or Sn L peaks were shown in Figs. 3 and 4, for the reduced A-Pt₁Sn₂/Al₂O₃ and C-Pt₁Sn₂/Al₂O₃ catalysts, respectively. The plots using all data, including the ones barely met the detectability criteria for

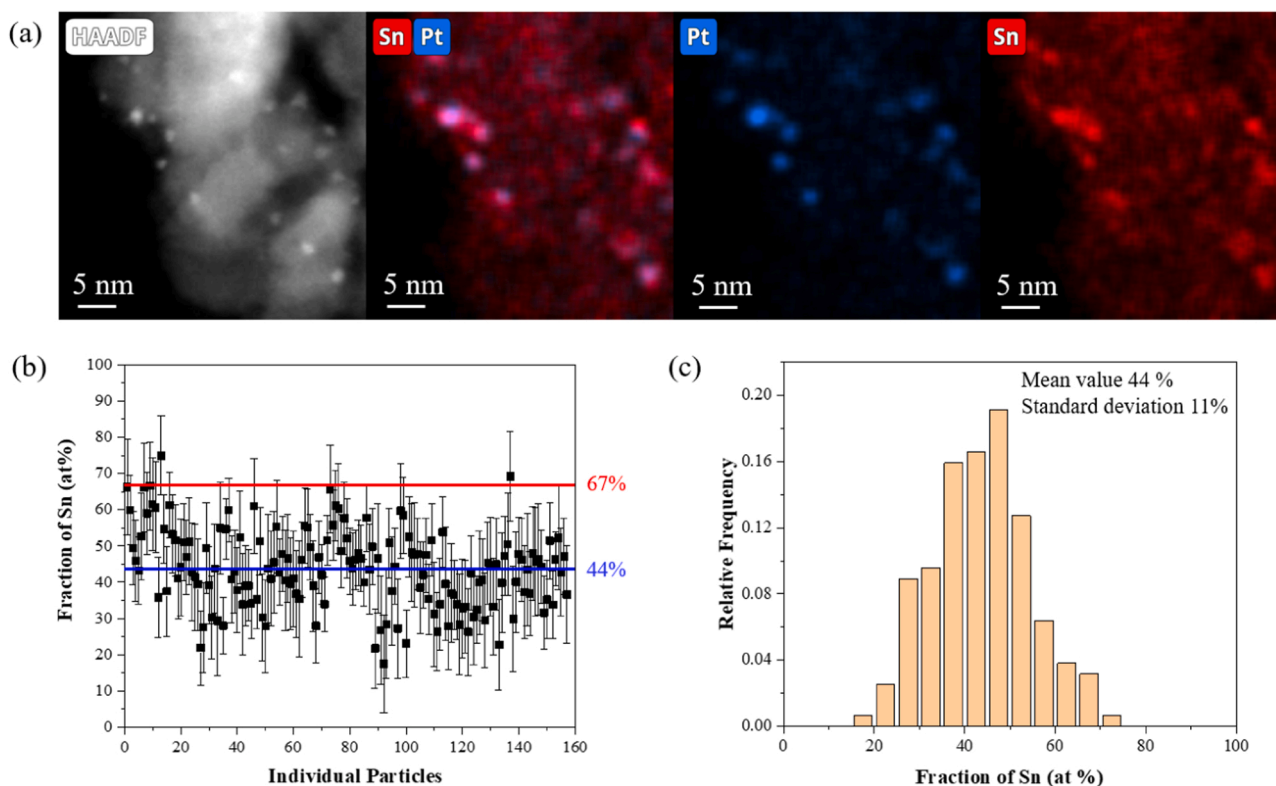


Fig. 4. Compositional analysis of the reduced C-Pt₁Sn₂/Al₂O₃ catalysts using STEM-X-EDS. (a) Representative dataset containing a HAADF image and the corresponding elemental maps obtained from the reduced C-Pt₁Sn₂/Al₂O₃ catalyst. (b) Compositions of individual PtSn nanoparticles (Sn at%) and (c) the corresponding composition distribution histogram. All the particles shown in this plot satisfy the statistical criteria, where both Pt M and Sn L peaks of each particles exceed three times the square root of the corresponding background intensities. (b) and (c) only include the particles with at least 100 photon counts in either Pt M or Sn L peaks. The more inclusive data summary containing the rest of particle spectra can be found in Fig. S18. Red line in (b): the overall Sn composition of the catalyst measured by ICP-OES; blue line in (b): average particle composition measured from STEM-X-EDS of individual nanoparticles. The error bars in (b) represent a confidence interval of 99%.

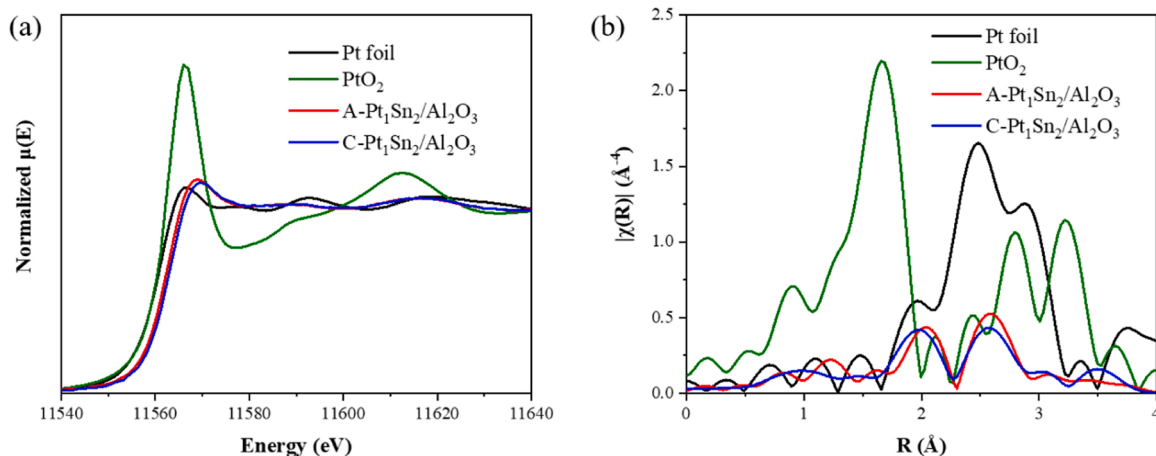


Fig. 5. *In situ* XAFS characterization of Pt L_{III}-edge for A-Pt₁Sn₂/Al₂O₃ and C-Pt₁Sn₂/Al₂O₃. (a) XANES and (b) Fourier transformed EXAFS of Pt foil, PtO₂ and reduced catalysts. The catalysts were *in situ* reduced by pure H₂ at 550 °C and cooled to room temperature to collect spectra. The data processing procedures were described in Text S1, and the fitting results could be found in Fig. S22 and S23.

Pt or Sn peaks were shown in Fig. S18. The findings were essentially the same that the composition distribution among particles in the reduced A-Pt₁Sn₂/Al₂O₃ was wide, and the Sn composition ranged from less than 30% to over 70%. On average, nanoparticles in A-Pt₁Sn₂/Al₂O₃ had a slightly higher Sn content (*i.e.*, 47%) compared to C-Pt₁Sn₂/Al₂O₃ (*i.e.*, 44%). The distribution was almost identical to that of the reduced C-Pt₁Sn₂/Al₂O₃ catalysts. In other words, the molecular complexes

surprisingly did not provide any noticeable benefits for controlling the particle compositions.

From the elemental maps shown in Figs. 3 and 4, we could also see that there are significant signals of Sn coming from the support area where no particles could be seen from the corresponding HAADF images. Indeed, if we integrated the signal from a larger support area, we could find clear signals of Sn, but not of Pt (Fig. S19). This indicated that

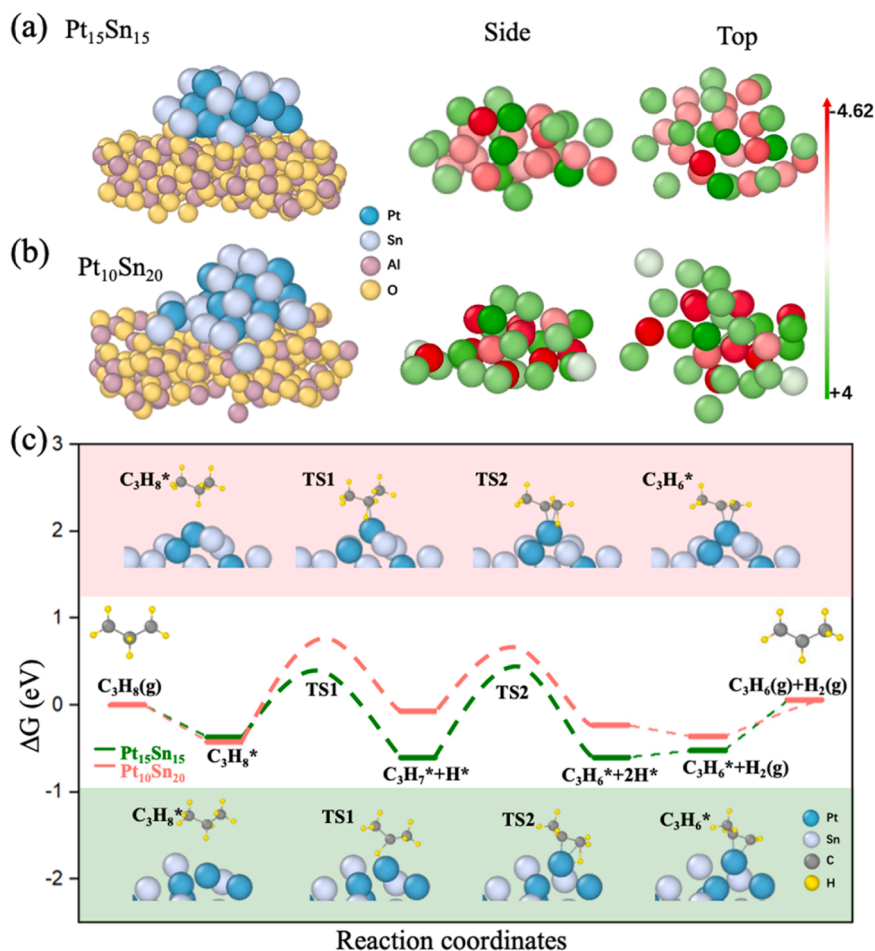


Fig. 6. Configurations of Pt-Sn clusters and energy diagram of PDH reaction. Structures of the (a) Pt₁₅Sn₁₅ and (b) Pt₁₀Sn₂₀ clusters on Al₂O₃ support after MD simulations and the corresponding charge state of the Pt (red) and Sn atoms (green). (c) Energy diagram for propane dehydrogenation to propylene.

the Sn species interacted strongly with the Al₂O₃ support, that is consistent with previous reports [17,18]. NH₃-TPD confirmed that some acid sites were eliminated after loading Pt-Sn species (Fig. S20), so a part of Sn was probably captured away from the clusters by the acid sites. This interaction could be the reason why we did not achieve a better control by introducing coordinated Pt-Sn precursors during the catalyst preparation. This also meant that the composition of the nanoparticles would have lower Sn content compared to the overall composition of the catalyst measured using bulk techniques, such as ICP-OES. And this was what we found in Figs. 3 and 4. Note that our control experiments showed that the weak signals from the support area would not affect the composition quantification of the supported particles. As shown in Fig. S21, the support area with a similar size integration window barely generated any signals above noise.

To further investigate the coordination environment of Pt, the two Pt₁Sn₂ catalysts were tested by *in situ* X-ray absorption fine structure (XAFS) of Pt L_{III} edge. After H₂ treatment, Pt was reduced to metallic state as shown in X-ray Absorption Near Edge Spectroscopy (XANES) (Fig. 5a), and Extended X-ray absorption fine structure (EXAFS) spectra verified the formation of Pt-Sn alloy in both samples (Fig. 5b, S22 and S23). The total coordination number of Pt in C-Pt₁Sn₂/Al₂O₃ was higher than that in A-Pt₁Sn₂/Al₂O₃, implying the larger particle size in the C-Pt₁Sn₂/Al₂O₃. Compared to the C-Pt₁Sn₂/Al₂O₃ catalyst, a higher Sn content in A-Pt₁Sn₂/Al₂O₃ could be estimated according to Pt-Pt and Pt-Sn coordination numbers obtained by EXAFS fitting [48], in agreement with the findings from electron microscopy. CO-DRIFT experiments (Fig. S24) also showed consistent results that both Pt sites were isolated by alloying with Sn in A-Pt₁Sn₂/Al₂O₃ and C-Pt₁Sn₂/Al₂O₃, with the

disappearance of the feature around 1800 cm⁻¹. The red-shift of the peak from 2078 cm⁻¹ for C-Pt₁Sn₂/Al₂O₃ to 2073 cm⁻¹ for A-Pt₁Sn₂/Al₂O₃ could be assigned to the increased charge transfer from Sn to Pt in the alloyed particles [14,24].

3.4. Theoretical Investigations

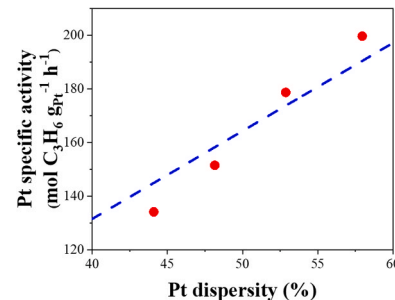
For sub-nanometer clusters, it was experimentally challenging to characterize the detailed structure of materials under experimental conditions due to the limitations of existing methods. Given that the overall catalytic activity mainly depended on the exposure of Pt atoms, we utilized MD simulations to understand the structures of Pt₁₅Sn₁₅ and Pt₁₀Sn₂₀ clusters around 1 nm diameter on the Al₂O₃(110) surface under 873 K and investigated their activity difference. Results indicated that due to the high temperature, the structure of Pt-Sn clusters changed greatly in 30 ps and displayed a liquid-like behavior, as shown in Fig. S25 and SI movies. Fig. 6a and b showed the structures of Pt-Sn clusters after reaching thermodynamic equilibrium (Fig. S26), where the flattened shape of cluster was due to the interactions between the cluster and support [49]. For both Pt₁₅Sn₁₅ and Pt₁₀Sn₂₀ clusters, the surface Pt sites were separated by Sn atoms, which donated electrons to Pt atoms according to the Bader charges in Fig. 6a and b (see exact values in Fig. S27). Because of the higher ratio of Sn in the Pt₁₀Sn₂₀ cluster, the charge state of Pt in the Pt₁₀Sn₂₀ cluster was -3.74, which was lower than the -2.36 in the Pt₁₅Sn₁₅ cluster.

To further investigate the catalytic differences between the two clusters, we selected two corresponding MD structures under thermal equilibrium and studied surface Pt sites with a similar charge state of

Table 2

Pt specific activity normalized by Pt dispersity measured by CO chemisorption. Relationship between Pt specific activity and Pt dispersity of the four PtSn catalysts was fitted linearly, with the intercept fixed at (0,0).

| Entry | Catalyst | Pt dispersity (%) | TOF (s^{-1}) |
|-------|---|-------------------|-------------------------|
| 1 | A-Pt/ Al_2O_3 | 57.4 | 5.2 |
| 2 | A-Pt ₁ Sn ₁ / Al_2O_3 | 52.9 | 18.3 |
| 3 | A-Pt ₁ Sn ₂ / Al_2O_3 | 58.0 | 18.7 |
| 4 | A-Pt ₁ Sn ₄ / Al_2O_3 | 48.2 | 17.0 |
| 5 | C-Pt ₁ Sn ₂ / Al_2O_3 | 44.1 | 16.5 |



about -2.0 for the dehydrogenation of propane to propylene. As described in Fig. 6c, the C-H breaking from propane was the rate-determine step (RDS) with an activation barrier of 1.17 eV for Pt₁₀Sn₂₀, while the RDS was the second C-H bond cleavage with an activation barrier of 1.04 eV for Pt₁₅Sn₁₅. Two other Pt sites with lower charge states were also studied (Fig. S28), and the results suggested that the fewer gained electrons, the better the catalytic activity of Pt sites. Overall, due to dynamic structural evolution, active Pt sites with similar activation energy barriers appeared in the Pt₁₅Sn₁₅ and Pt₁₀Sn₂₀ clusters, and clusters with a Pt:Sn ratio of 1:1 possessed more active sites, which led to better catalytic activity and higher propylene yield for the Pt₁₅Sn₁₅ cluster.

Note that Fig. 6c included the Gibbs free energy corrections only for the gaseous species, as treated in literature [50]. However, the qualitative results remain the same (Fig. S29) if the Gibbs free energy corrections were added to both the gaseous species and reaction intermediates [51–53].

3.5. Discussion of the origin of the high PDH activities for the A-Pt₁Sn₂/ Al_2O_3 catalysts

The finding that the composition distribution of our best A-Pt₁Sn₂/ Al_2O_3 was very similar to that of the C-Pt₁Sn₂/ Al_2O_3 catalyst was a surprising one. Although theoretical works, such as the works by Liu *et al.* [53] and Yang *et al.* [54], and our own simulations discussed above, all suggested that there should exist an optimum Pt-Sn composition, it remained difficult to experimentally achieve controlled synthesis so that only particles with the optimum composition existed. At least, we could not attribute the high activities observed in our best catalyst to the particle compositions.

Our kinetics measurement suggested that catalysts with different overall compositions had rather similar apparent activation energies, which were usually dominated by the first dehydrogenation step of propane. This indicated that these catalysts shared similar active sites for the dehydrogenation reaction. The conventional wisdom [55] was that dehydrogenation on Pt was structure-insensitive, meaning that the reaction took place on a single site and less influenced by the local environment of the sites. Although A-Pt₁Sn₂/ Al_2O_3 catalyst had a 0.76 nm average size, which was only about 0.6 nm smaller than that of C-Pt₁Sn₂/ Al_2O_3 , the number of exposed Pt sites could already be significantly different between the two at this size range. We used CO chemisorption to estimate the number of Pt sites that were accessible in the reduced catalysts. Indeed a good correlation was observed between Pt specific activity and Pt dispersity, and the turn-over frequency remained at the same level for the PtSn/ Al_2O_3 catalysts (Table 2), implying that the overall catalytic activity primarily depended on the exposure of Pt. Similar results were recently reported by Murata *et al.* [24] when studying dehydrogenation of methylcyclohexane.

We could infer that the main benefit of our synthesis route with the molecular complexes of Pt and Sn was to achieve a better particle size control, over the ones prepared using impregnation. It did not offer much benefit over composition control, except that it allowed catalysts with higher Sn:Pt ratio to be prepared without forming unwanted large particles. Interestingly, even if we knew that the catalyst had some Pt rich particles, the PtSn catalysts all showed superior C₃H₆ selectivities over the pure Pt catalyst. This suggested that, at least for this size range, PtSn nanoparticles could have a wide composition range to be effective in terms of switching-off side reactions for PDH.

4. Conclusions

In summary, we investigated the industrially important PtSn/ Al_2O_3 catalysts prepared with uniform particle sizes (~ 1 nm) and varied compositions using molecular complexes of Pt(II) and Sn(II). Our best catalyst, with a Sn:Pt ratio of around 2, exhibited a high initial propylene productivity of about 1.1 mol C₃H₆ (g catalyst)⁻¹ h⁻¹. Under optimized reaction condition, this catalyst could also have a low deactivation rate of about 0.009 h⁻¹.

Through comprehensive electron microscopy studies, including particle size analysis and compositional analysis of individual particles, we discovered significant compositional variations within the PtSn/ Al_2O_3 catalysts that were highly active and selective for PDH. This indicated that our new synthesis method did not offer a clear advantage over the catalyst prepared without molecular complexes. Instead, our method facilitated size-controlled synthesis over a wider range of Sn:Pt ratios compared to the conventional impregnation method. We found that the dehydrogenation activities seemed to correlate well with the Pt dispersity measured from CO chemisorption, indicating the structure-insensitive nature of the dehydrogenation reaction applied in these ultrasmall Pt-Sn nanoparticles. The presence of a significant fraction of Pt-rich particles in the catalyst did not appear to impact the selectivity of the reaction towards propylene. This suggested that, at least within this size range, PtSn nanoparticles could have a wide composition range while remaining effective in minimizing side reactions in the PDH process. These insights into the industrially important PtSn/ Al_2O_3 catalysts would not have been possible without the compositional analysis of the catalysts using electron microscopy.

CRedit authorship contribution statement

C. Xu, A. Howe and Q. He conceived the idea and led the project. C. Xu carried out the catalyst synthesis, testing and most of the characterizations with the help from A. Howe, B. Zhao, S. Lu and Y. Du. M. Tian from C. He's group obtained some early results for this project during her 1-year visit to Q. He's lab. S. Xi led the *in situ* XAFS studies at SSLS. L. Ma carried out some preliminary ex situ XAFS studies for both Pt L_{III} and

Sn K edges. S. Tan, B. Yao obtained the STEM imaging and X-EDS data and carried out the data analysis under the supervision of Q. He and S. Dai. A. Wade obtained some preliminary X-EDS data as the proof-of-principle. Y. Tang led the theoretical investigation using DFT and AIMD under the supervision of G. Luo. X. Fu and J. Shi carried out the ICP-OES analysis of the catalysts under the supervision of J. Lu. C. Xu, Y. Tang, S. Tan and Q. He prepared the paper and all authors participated in the discussion and helped to polish the manuscript.

Declaration of Competing Interest

The authors declare no competing financial interests.

Data Availability

Data will be made available on request.

Acknowledgements

Q. He acknowledges the support from National Research Foundation (NRF) Singapore, under its NRF Fellowship (NRF-NRFF11-2019-0002). G. Luo acknowledges the support from Guangdong Provincial Key Laboratory of Computational Science and Material Design (Grant No. 2019B030301001), the Introduced Innovative R&D Team of Guangdong (Grant No. 2017ZT07C062), the Shenzhen Science and Technology Innovation Commission (No. JCYJ20200109141412308), the National Foundation of Natural Science, China (No. 52273226). All the calculations were carried out on the Taiyi cluster supported by the Center for Computational Science and Engineering of Southern University of Science and Technology. S. Dai acknowledges the support from the Science and Technology Commission of Shanghai Municipality (22ZR1415700), Shanghai Rising-Star Program (20QA1402400), and the Fundamental Research Funds for the Central Universities. J. Lu acknowledges the support from Agency for Science, Technology and Research (A*STAR) under its MTC IRG Grant (M22K2c0082). Mingjiao Tian acknowledges the financial support from the China Scholarship Council.

Appendix A. Supporting information

Supplementary data associated with this article can be found in the online version at [doi:10.1016/j.apcatb.2023.123285](https://doi.org/10.1016/j.apcatb.2023.123285).

References

- [1] R. Ferrando, J. Jellinek, R.L. Johnston, Nanoalloys: from theory to applications of alloy clusters and nanoparticles, *Chem. Rev.* 108 (2008) 845–910.
- [2] L. Liu, A. Corma, Bimetallic sites for catalysis: from binuclear metal sites to bimetallic nanoclusters and nanoparticles, *Chem. Rev.* (2023).
- [3] C. Kiely, Electron microscopy: new views of catalysts, *Nat. Mater.* 9 (2010) 296–297.
- [4] R.E. Lakis, C.E. Lyman, H.G. Stenger, Alumina-supported Pt-Rh catalysts: I. Microstructural characterization, *J. Catal.* 154 (1995) 261–275.
- [5] L. Bednarova, C.E. Lyman, E. Rytter, A. Holmen, Effect of support on the size and composition of highly dispersed Pt–Sn particles, *J. Catal.* 211 (2002) 335–346.
- [6] M. Sankar, Q. He, M. Morad, J. Pritchard, S.J. Freakley, J.K. Edwards, S.H. Taylor, D.J. Morgan, A.F. Carley, D.W. Knight, C.J. Kiely, G.J. Hutchings, Synthesis of stable ligand-free gold-palladium nanoparticles using a simple excess anion method, *ACS Nano* 6 (2012) 6600–6613.
- [7] S. Liu, I. Gow, T. Davies, A. Barnes, M. Sankar, X. Gong, A.G.R. Howe, M. Dixon, G. J. Hutchings, C.J. Kiely, Q. He, Probing composition distributions in nanoalloy catalysts with correlative electron microscopy, *J. Mater. Chem. A Mater. Energy Sustain.* 8 (2020) 15725–15733.
- [8] H.L. Xin, J.A. Mundy, Z. Liu, R. Cabezas, R. Hovden, L.F. Kourkoutis, J. Zhang, N. P. Subramanian, R. Makharia, F.T. Wagner, D.A. Muller, Atomic-resolution spectroscopic imaging of ensembles of nanocatalyst particles across the life of a fuel cell, *Nano Lett.* 12 (2012) 490–497.
- [9] J.J.H.B. Sattler, J. Ruiz-Martinez, E. Santillan-Jimenez, B.M. Weckhuysen, Catalytic dehydrogenation of light alkanes on metals and metal oxides, *Chem. Rev.* 114 (2014) 10613–10653.
- [10] S. Chen, X. Chang, G. Sun, T. Zhang, Y. Xu, Y. Wang, C. Pei, J. Gong, Propane dehydrogenation: catalyst development, new chemistry, and emerging technologies, *Chem. Soc. Rev.* 50 (2021) 3315–3354.
- [11] J. Wu, Z. Peng, A.T. Bell, Effects of composition and metal particle size on ethane dehydrogenation over Pt_xSn_{100-x}/Mg (Al) O (70 ≤ x ≤ 100), *J. Catal.* 311 (2014) 161–168.
- [12] J. Zhang, Y. Deng, X. Cai, Y. Chen, M. Peng, Z. Jia, Z. Jiang, P. Ren, S. Yao, J. Xie, Tin-assisted fully exposed platinum clusters stabilized on defect-rich graphene for dehydrogenation reaction, *ACS Catal.* 9 (2019) 5998–6005.
- [13] G.J. Siri, J.M. Ramallo-López, M.L. Casella, J.L. Fierro, F.G. Requejo, O.A. Ferretti, XPS and EXAFS study of supported PtSn catalysts obtained by surface organometallic chemistry on metals: application to the isobutane dehydrogenation, *Appl. Catal. A: Gen.* 278 (2005) 239–249.
- [14] Q. Wang, D. Tichit, F. Meunier, H. Guesmi, Combined DRIFTS and DFT study of CO adsorption and segregation modes in Pt–Sn nanoalloys, *J. Phys. Chem. C* 124 (2020) 9979–9989.
- [15] M.S. Kumar, D. Chen, A. Holmen, J.C. Walmsley, Dehydrogenation of propane over Pt-SBA-15 and Pt-Sn-SBA-15: Effect of Sn on the dispersion of Pt and catalytic behavior, *Catal. Today* 142 (2009) 17–23.
- [16] H.N. Pham, J.J. Sattler, B.M. Weckhuysen, A.K. Datye, Role of Sn in the regeneration of Pt/γ-Al₂O₃ light alkane dehydrogenation catalysts, *ACS Catal.* 6 (2016) 2257–2264.
- [17] S.R. Adkins, B.H. Davis, The chemical state of tin in platinum-tin-alumina catalysts, *J. Catal.* 89 (1984) 371–379.
- [18] J. Luy, S. de Miguel, G. Baronetti, O. Scelza, A. Castro, Performance of Pt– Sn/ Al₂O₃– Cl catalysts in isopropanol decomposition, *React. Kinet. Catal. Lett.* 32 (1986) 239–244.
- [19] G. Wang, H. Zhang, H. Wang, Q. Zhu, C. Li, H. Shan, The role of metallic Sn species in catalytic dehydrogenation of propane: active component rather than only promoter, *J. Catal.* 344 (2016) 606–608.
- [20] B. Werghi, L. Wu, A.M. Ebrahim, M. Chi, H. Ni, M. Carnello, S.R. Bare, Selective catalytic behavior induced by crystal-phase transformation in well-defined bimetallic Pt-Sn nanocrystals, *Small* 19 (2023), e2207956.
- [21] X. Gao, W. Xu, X. Li, J. Cen, Y. Xu, L. Lin, S. Yao, Non-oxidative dehydrogenation of propane to propene over Pt-Sn/Al₂O₃ catalysts: Identification of the nature of active site, *Chem. Eng. J.* 443 (2022), 136393.
- [22] P. Pregosin, H. Rüegger, 119Sn and 195Pt NMR spectroscopy of SnCl₃– complexes of platinum and palladium. Some chemistry of the complexes (Ph₄P)₂ [PtCl₄] and [Pt (μ-Cl) Cl (PEt₃)]₂ with SnCl₂, *Inorg. Chim. Acta* 86 (1984) 55–60.
- [23] J. Young, R. Gillard, G. Wilkinson, 992. Complexes of ruthenium, rhodium, iridium, and platinum with tin (II) chloride, *J. Chem. Soc. (Resume)* (1964) 5176–5189.
- [24] K. Murata, N. Kurimoto, Y. Yamamoto, A. Oda, J. Ohyama, A. Satsuma, Structure–property relationships of Pt–Sn nanoparticles supported on Al₂O₃ for the dehydrogenation of methylcyclohexane, *ACS Appl. Nano Mater.* 4 (2021) 4532–4541.
- [25] Y. Du, Y. Zhu, S. Xi, P. Yang, H.O. Moser, M.B. Breese, A. Borgna, XAFCA: a new XAFS beamline for catalysis research, *J. Synchrotron Radiat.* 22 (2015) 839–843.
- [26] B. Ravel, M. Newville, ATHENA, ARTEMIS, HEPHAESTUS: data analysis for X-ray absorption spectroscopy using IFEFFIT, *J. Synchrotron Radiat.* 12 (2005) 537–541.
- [27] G. Kresse, J. Furthmüller, Efficiency of ab-initio total energy calculations for metals and semiconductors using a plane-wave basis set, *Comput. Mater. Sci.* 6 (1996) 15–50.
- [28] G. Kresse, J. Furthmüller, Efficient iterative schemes for ab initio total-energy calculations using a plane-wave basis set, *Phys. Rev. B* 54 (1996) 11169.
- [29] J.P. Perdew, Y. Wang, Accurate and simple analytic representation of the electron-gas correlation energy, *Phys. Rev. B* 45 (1992) 13244.
- [30] S. Grimme, J. Antony, S. Ehrlich, H. Krieg, A consistent and accurate ab initio parametrization of density functional dispersion correction (DFT-D) for the 94 elements H–Pu, *J. Chem. Phys.* 132 (2010), 154104.
- [31] G. Kresse, D. Joubert, From ultrasoft pseudopotentials to the projector augmented-wave method, *Phys. Rev. B* 59 (1999) 1758.
- [32] R. Jinnouchi, F. Karsai, C. Verdi, R. Asahi, G. Kresse, Descriptors representing two- and three-body atomic distributions and their effects on the accuracy of machine-learned inter-atomic potentials, *J. Chem. Phys.* 152 (2020), 234102.
- [33] S. Nosé, A unified formulation of the constant temperature molecular dynamics methods, *J. Chem. Phys.* 81 (1984) 511–519.
- [34] W.G. Hoover, Canonical dynamics: equilibrium phase-space distributions, *Phys. Rev. A* 31 (1985) 1695.
- [35] H. Cai, G. Liu, P. Qiu, G. Luo, Structural feature in dynamical processes accelerated transition state calculations, *J. Chem. Phys.* 158 (2023).
- [36] G. Henkelman, B.P. Uberuaga, H. Jónsson, A climbing image nudged elastic band method for finding saddle points and minimum energy paths, *J. Chem. Phys.* 113 (2000) 9901–9904.
- [37] R.F. Bader, Atoms in molecules, *Acc. Chem. Res.* 18 (1985) 9–15.
- [38] G. Henkelman, A. Arnaldsson, H. Jónsson, A fast and robust algorithm for Bader decomposition of charge density, *Comput. Mater. Sci.* 36 (2006) 354–360.
- [39] A.H. Motagamwala, R. Almallahi, J. Wortman, V.O. Igenegbai, S. Linic, Stable and selective catalysts for propane dehydrogenation operating at thermodynamic limit, *Science* 373 (2021) 217–222.
- [40] G.T. Baronetti, S.R. de Miguel, O.A. Scelza, M.A. Fritzler, A.A. Castro, PtSn/Al₂O₃ catalysts: Studies of the impregnation step, *Appl. Catal.* 19 (1985) 77–85.
- [41] L. Qi, M. Babucci, Y. Zhang, A. Lund, L. Liu, J. Li, Y. Chen, A.S. Hoffman, S.R. Bare, Y. Han, Propane dehydrogenation catalyzed by isolated Pt atoms in— SiO₂–OH nests in dealuminated zeolite beta, *J. Am. Chem. Soc.* 143 (2021) 21364–21378.
- [42] S. Gómez-Quero, T. Tsoufis, P. Rudolf, M. Makkee, F. Kapteijn, G. Rothenberg, Kinetics of propane dehydrogenation over Pt–Sn/Al₂O₃, *Catal. Sci. Technol.* 3 (2013) 962–971.

- [43] Q. Li, Z. Sui, X. Zhou, D. Chen, Kinetics of propane dehydrogenation over Pt-Sn/Al₂O₃ catalyst, *Appl. Catal. A: Gen.* 398 (2011) 18–26.
- [44] H. Liu, J. Zhou, T. Chen, P. Hu, C. Xiong, Q. Sun, S. Chen, T.W.B. Lo, H. Ji, Isolated Pt species anchored by hierarchical-like heteroatomic Fe-silicalite-1 catalyze propane dehydrogenation near the thermodynamic limit, *ACS Catal.* 13 (2023) 2928–2936.
- [45] R.F. Egerton, P. Li, M. Malac, Radiation damage in the TEM and SEM, *Micron* 35 (2004) 399–409.
- [46] N.J. Zaluzec, Quantitative assessment and measurement of X-ray detector performance and solid angle in the analytical electron microscope, *Microsc. Micro* 28 (2022) 83–95.
- [47] D.B. Williams, C.B. Carter, *Transmission Electron Microscopy*, Springer Science & Business Media, 2009.
- [48] N.V. Srinath, H. Poelman, L. Buelens, J. Dendooven, M.-F. Reyniers, G.B. Marin, V. V. Galvita, Behaviour of platinum-tin during CO₂-assisted propane dehydrogenation: insights from quick X-ray absorption spectroscopy, *J. Catal.* 408 (2022) 356–371.
- [49] L. Shi, G.M. Deng, W.C. Li, S. Miao, Q.N. Wang, W.P. Zhang, A.H. Lu, Al₂O₃ nanosheets rich in pentacoordinate Al³⁺ ions stabilize Pt-Sn clusters for propane dehydrogenation, *Angew. Chem. Int. Ed.* 54 (2015) 13994–13998.
- [50] H. Wan, L. Qian, N. Gong, H. Hou, X. Dou, L. Zheng, L. Zhang, L. Liu, Size-dependent structures and catalytic properties of supported bimetallic PtSn catalysts for propane dehydrogenation reaction, *ACS Catal.* 13 (2023) 7383–7394.
- [51] Z. Li, L. Yu, C. Milligan, T. Ma, L. Zhou, Y. Cui, Z. Qi, N. Libretto, B. Xu, J. Luo, Two-dimensional transition metal carbides as supports for tuning the chemistry of catalytic nanoparticles, *Nat. Commun.* 9 (2018) 5258.
- [52] S. Zha, G. Sun, T. Wu, J. Zhao, Z.-J. Zhao, J. Gong, Identification of Pt-based catalysts for propane dehydrogenation via a probability analysis, *Chem. Sci.* 9 (2018) 3925–3931.
- [53] Y. Liu, X. Zong, A. Patra, S. Caratzoulas, D.G. Vlachos, Propane dehydrogenation on Pt x Sn y (x, y ≤ 4) Clusters on Al₂O₃ (110), *ACS Catal.* 13 (2023) 2802–2812.
- [54] M.-L. Yang, Y.-A. Zhu, X.-G. Zhou, Z.-J. Sui, D. Chen, First-principles calculations of propane dehydrogenation over PtSn catalysts, *Acs Catal.* 2 (2012) 1247–1258.
- [55] M. Boudart, Heterogeneous catalysis by metals, *J. Mol. Catal.* 30 (1985) 27–38.